

CC BY-NC-ND 4.0 DEED Attribution-NonCommercial-NoDerivs 4.0 International

<https://creativecommons.org/licenses/by-nc-nd/4.0/>

<https://doi.org/10.1016/j.nanoen.2021.106482>

Access to this work was provided by the University of Maryland, Baltimore County (UMBC) ScholarWorks@UMBC digital repository on the Maryland Shared Open Access (MD-SOAR) platform.

Please provide feedback

Please support the ScholarWorks@UMBC repository by emailing scholarworks-group@umbc.edu and telling us what having access to this work means to you and why it's important to you. Thank you.

Effect of Particle-Size Distribution and Pressure-Induced Densification on the Microstructure and Properties of Printable Thermoelectric Composites and High Energy Density Flexible Devices

Priyanshu Banerjee¹, Jiyuan Huang¹, Rohan B. Ambade², Eunhwa Jang¹, Mortaza Saeidi-Javash³,
Yanliang Zhang³, Deepa Madan^{1,*}

¹Department of Mechanical Engineering, University of Maryland Baltimore County, Baltimore, 21250

² Department of Organic and Nano Engineering, Hanyang University, Seoul 04763, Republic of Korea

³ Department of Aerospace and Mechanical Engineering, University of Notre Dame, Notre Dame, IN, 46556, USA

*Corresponding Author, E-mail: deemadan@umbc.edu

Abstract

To address the global demand for low-cost, flexible thermoelectric generators (TEGs), this work describes a novel, energy-efficient method of controlling the composite microstructure and resulting thermoelectric (TE) properties of p-type composite films. Combining (1) a small amount of naturally occurring binder that is sufficient to hold TE particles together without significantly decreasing electrical conductivity and (2) a wide distribution of heterogeneous (micro and nano) particles tightly packed on (3) application of mechanical pressure at (4) low-temperature curing for a short duration, this method yields big grains larger than the mean free path for charge carriers (for high electrical conductivity) and nano features smaller than the mean free path for phonons (for low thermal conductivity). The best properties were achieved with 0.05 wt% of chitosan binder, heterogeneous-sized TE particles (100-mesh $\text{Bi}_{0.5}\text{Sb}_{1.5}\text{Te}_3$), 200 MPa applied uniaxial pressure, and curing at 150 °C for 30 minutes to densify the as-deposited films. The 100-mesh chitosan-BST composite film achieved a ZT of 0.7, comparable to the best reported ZT of printed p-type TE films, but without using high-temperature and long-duration curing. The power output of our best-reported scalable 3-leg-BST TEG was 58 μW . The corresponding power density was 5.72 mW/cm^2 at a temperature difference of 38 K, significantly higher than the best reported values for single-leg TEGs. Furthermore, the flexibility of this prototype was performed by successfully bending at a 3-cm radius for 1000 cycles, thus demonstrating a high potential to be used as self-sufficient batteries for next-generation wearable devices and wireless sensor network applications.

Keywords: Composite thermoelectric film, Bismuth Antimony Telluride, mechanical pressure, naturally occurring chitosan, stencil printing, heterogenous particle size distribution

1. Introduction

Global energy consumption is increasing rapidly each year, leading researchers to investigate alternative energy-harvesting devices. Thermoelectric generators (TEGs) can convert waste heat to useful electrical energy [1–3]. TEGs are also reliable, scalable, and essentially maintenance-free devices [4–6]. Additive manufacturing of flexible thermoelectric generators (TEGs) promises to deliver low-cost, and high-energy-density devices that can potentially charge batteries by harvesting otherwise waste heat from planar and non-planar surfaces [7–9]. The irony is that additive manufacturing methods involve energy-intensive (long-duration and high-temperature) curing processes, and devices suffer from low performance (primarily due to the low thermoelectric performance of thermoelectric-polymer composite films).

Printed films suffer from low performance for two main reasons: first, the presence of insulating binder and/or poor interfacial connection between active particles, which results in lower electrical conductivity; and second, the interdependence of electron- and phonon transport properties in composite films, which limits the ability to achieve both high electrical conductivity and low thermal conductivity simultaneously. The previous reports on TE demonstrated that a higher-mass loading of insulating polymer binder in composite films (typically 20-30 wt%) causes a significant loss of electrical conductivity due to poor connections between thermoelectric particles. Therefore, the thermoelectric performance (ZT) of printed composite films is much lower than bulk thermoelectric materials [10–14]. Various approaches have been proposed to enhance the ZT of composite films, including the use of removable binders and conductive polymers [15–19]. However, pores left behind after the removable binder and solvent

evaporation cause poor interfacial connections between TE particles [20]. In addition, the poor adhesion strength of conductive polymers also limits the weight loading of inorganic particles in the films [21,22].

The naturally-occurring chitosan has excellent mechanical strength therefore a minimal amount of the chitosan is sufficient to hold the TE particles together, making it an excellent binder [23–31]. Chitosan is not a water-based binder; therefore, it does not rapidly oxidize the composite films [23,24]. To enhance the thermoelectric properties of composite films, whether or not they use traditional or removable binders, a long-duration (up to 18 h) and high-temperature (350–500 °C) sintering of the composite films is usually performed [14–21]. Although the high-temperature sintering of as-printed composite films enhances their thermoelectric performance, the process is energy-intensive and unsuitable for large-scale and environmentally-friendly additive manufacturing of flexible thermoelectric devices [5]. Therefore, uniaxial pressure instead of high-temperature curing to modify the composite microstructure is an attractive energy-efficient approach. Uniaxial pressure, together with high-temperature sintering, has been previously used to enhance the properties of thermoelectric composite films synthesized with removable binders [15,16,20]. Our unique approach promises to eliminate the use of state-of-the-art high-temperature and long-duration curing methods. The presence of a small (<50%) wt% of fine (nanoscale) particles among coarse (microscale) particles helps achieve better packing density and, therefore, resulted in higher electrical conductivity in bulk samples [32–35]. However, the presence of too many fine particles (>50 wt%) creates too many grain boundaries, which can reduce electrical conductivity [32–35].

However, to the best of our knowledge, no reported study has explored the synergistic effect of combining a small amount of binder, heterogenous particle-size distribution, and

applied pressure densification to control the composite microstructure and the resulting TE properties of p-type composite films. The synergetic approach achieved a ZT of 0.7 for $\text{Bi}_{0.5}\text{Sb}_{1.5}\text{Te}_3$ (BST) films prepared using heterogeneous-sized particles (BST-100-mesh), 0.05 wt% of chitosan binder, at low-temperature (150 °C), short-duration (30 min) curing, and 200 MPa applied pressure to densify as-deposited film. A wide distribution of mixed-sized particles, when subjected to external pressure, form big grains (plastic deformation) which have large mean free paths to allow charge carriers to flow easily and cause less scattering at the grain boundary (**Fig. 1**). The carrier mobility and electrical conductivity of these composite films are comparable to the best reported printable TE films and bulk TE samples, but without using high-temperature sintering and long hours of annealing [14–20,36]. Furthermore, the size and density of nano-sized TE particles, defects, and interfaces distributed among large grains of active particles can increase the interfacial thermal resistance and phonon scattering, helping to reduce the thermal conductivity of the composite films without significantly affecting their electrical conductivity (**Fig. 1**). The highly scalable and flexible 3-leg p-type TEG device was stencil-printed using BST-100 mesh composite ink and achieved a maximum power output of 58 μW at a temperature difference (ΔT) of 38 K. The non-spacing power density was determined to be 5.72 mW/cm^2 which is higher than all reported power density results for single-leg TEG devices [20,37–39].

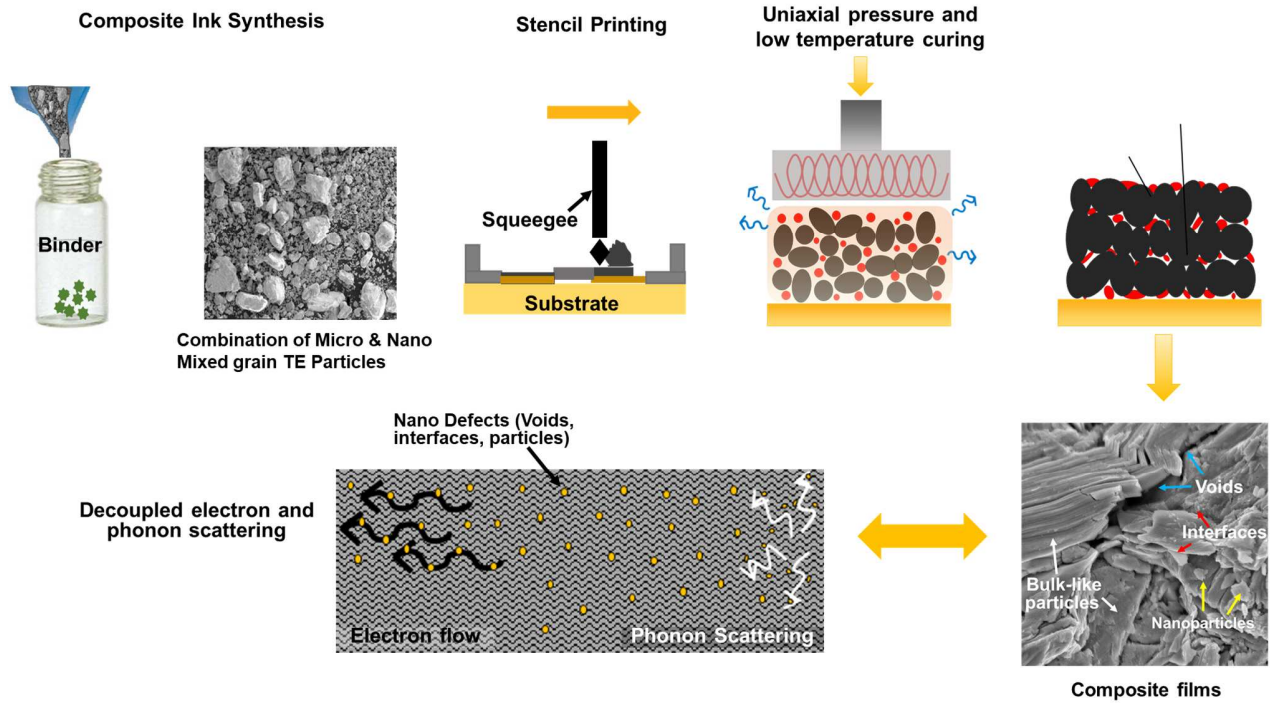


Fig. 1 Schematic illustration of a novel energy-efficient method to increase electrical conductivity (due to big grain features larger than the electron transport mean flow path) and decrease thermal conductivity (due to the presence of nano defects and thermal interfaces) in thermoelectric composite films using (1) heterogenous particle-size distribution, (2) small amount of binder, (3) curing at 150 °C for 30 minutes and, (4) uniaxial pressure.

2. Results and Discussion

2.1 TE Particle Size and Chitosan Binder Analysis

Fig. 2a shows the X-ray powder diffraction (XRD) patterns of BST-100-mesh powder, chitosan powder, and chitosan-BST-100 composite film. The XRD of chitosan-BST composite films shows the peak corresponding to both chitosan and BST and consistent with the standard database of BST and chitosan peaks(JCPDS 49-1713) [38,40,41]. The Raman spectra show (**Fig. 2b**) dominant peaks corresponding to BST phonon vibration modes (66, 108, 168 cm^{-1}) in BST powder and film and indicate the presence of chitosan with the presence of D-band (1370

cm^{-1}) and G-band (1570 cm^{-1}) [42,43]. XRD and Raman analysis show that chitosan and BST are present in chitosan-BST composite films. The heterogeneous particle-size distribution for commercial BST-100 and BST-325 particles was calculated using SEM images (**Fig. 2f-g**) and ImageJ software. **Fig. 2h-i** shows the approximate particle count of BST-100 and BST-325 thermoelectric particles vs. particle size. Smaller mesh size means that particles were filtered using sieves with larger openings. The standard “100-mesh” size means that particles were filtered using a sieve with 149-micron openings. Filtering through 149-micron openings ensures that almost all the particles are smaller than 149 microns. Note that filtering through 149-micron openings does not guarantee that all particles will be smaller than 149 microns because particles can have various 3D shapes (e.g., cylinders, cones, ellipses, prisms). Although almost all the particles in the 100-mesh sample are smaller than 149 microns, there are a small number of larger particles present as well (**Fig. 2f-h**). Similarly, the 325-mesh size means that the particles have been filtered using a sieve with 44-micron openings. It is expected that some of these particles will be larger than 44 microns, as seen in **Fig. 2g-i**. BST-100 mesh powder has larger micro-sized particles (~150 microns) than BST-325 mesh powder (~44 microns). These larger particles facilitate charge carriers' larger mean free path and contribute to high charge carrier mobility and electrical conductivity. **Fig. S4a** shows chitosan powder and BST-chitosan films remains thermally stable up to 200 °C and 120 °C is sufficient for curing films respectively [44,45].

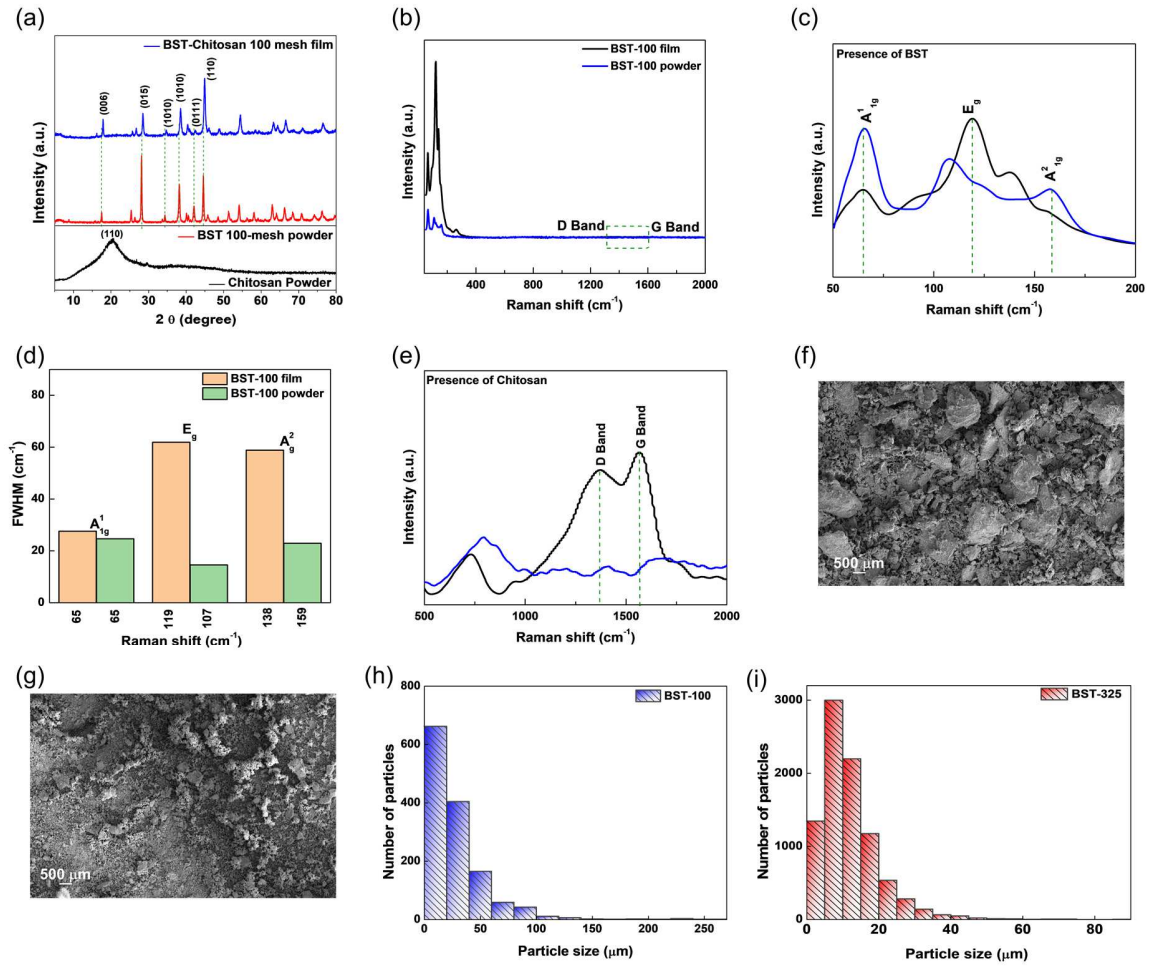


Fig. 2. (a) XRD patterns of BST powder, chitosan powder, and chitosan-BST composite film, (b) Raman spectra of BST powder and chitosan-BST composite films, (c) Raman spectra of BST powder and composite films showing peaks related to BST, (d) Raman spectra show the D and G band in BST composite films confirming the presence of chitosan, (e) FWHM for BST-100 powder and BST-100 composite films confirming the E_g peak shift in BST film with higher intensity, (f, g) SEM images of BST-100 and BST-325 particles, (h, i) BST-100 and BST-325 particle count vs. particle size.

2.3 Electrical Conductivity

Fig. 3 shows the electrical conductivity, Seebeck coefficient, charge carrier concentration, mobility, and power factor of p-type chitosan-BST (100-mesh and 325-mesh) TE

composite films with respect to the weight ratio of binder to TE particles (1:500, 1:2000, 1:5000, and 1:7000). The TE-chitosan composite films are composed of the conductive phase (active p-type BST TE particles) and the dispersion phase (insulating chitosan binder). When the BST TE phase reaches the percolation threshold, the electrical conductivity increases drastically due to the formation of continuous charge transport paths inside the chitosan binder in composites. However, once the TE particles attain a percolation threshold, increasing the amount of conductive TE particles in the chitosan-TE composite films does not result in a remarkable increase in electrical conductivity [46–49]. **Fig. S5** shows the variation of electrical conductivity for chitosan BST-100 composite films at different binder-to-particle weight ratios. The electrical conductivity values become stable at ratios of 1:500 and higher. Therefore, we conclude that a binder-to-particle weight ratio of 1:500 is close to the percolation threshold. The electrical conductivity did not show much variation resulting from changes to the binder-to-particle weight ratio (1:500, 1:2000, 1:5000, and 1:7000) for BST-100 and BST-325 composite films (**Fig. 3a**). When the binder-to-particle weight ratio was lower than 1:500, the electrical conductivity was one order lower for BST-100 and BST-325 films. The highest electrical conductivity (600 S/cm) was observed at a binder-to-particle weight ratio of 1:2000 for BST-100 and BST-325 films. Thus, for discussion purposes in this manuscript, we have considered the TE results of chitosan-TE composite films with a 1:2000 binder-to-particle weight ratio.

The best average electrical conductivity (600 S/cm) for the p-type chitosan-BST-100 TE composite films (1:2000 binder-to-particle weight ratio) was achieved by reducing the amount of binder (0.05 wt%) (**Fig. 3a**). This electrical conductivity value is one order lower than bulk BST (1100-1200 S/cm) [36]. The average electrical conductivity for BTS-325 films (1:2000 binder-to-particle weight ratio) was 170 S/cm. The high conductivity value for BST-100 is due to the

synergetic effects of a small amount of binder (0.05 wt%), distribution of varying particle sizes (submicron to 350 microns), and uniaxial applied mechanical pressure (200 MPa). In addition, the effect of heterogeneous particle-size distribution is investigated (**Fig. 2e-f**). The BST-100 composite films have a wider distribution of particle sizes (submicron to 350 microns) than BST-325 films (submicron to 80 microns) (**Fig. 2e-f**). Therefore, for the same binder-to-particle weight ratio (1:2000) and the same unit area, BST-100 composite films have a combination of the biggest and small particles. The presence of fine (nanoscale) particles among coarse (microscale) particles helps achieve better packing density, fewer grain boundaries, high mobility, and higher electrical conductivity [33,34].

The SEM image (**Fig. 3f**) of BST-100 films shows the mixed grains of varying particle size (that were initially separated by an insulating binder, pores, and voids) were merged (plastically deformed) and came in electrical contact on the application of pressure. The grains in contact increased the mean free path for charge carriers and facilitated hole transport, resulting in high mobility [33,34,50]. The BST-100 TE composite films have fewer grain boundaries, higher mobility (**Fig. 3d**), and higher electrical conductivity (**Fig. 3a**) than BST-325. The BST-325 composite films have more grains, grain boundaries, and pores (indicated by yellow arrows), as shown in **Fig. 3g**. These factors contribute to more grain boundary scattering and lower electrical conductivity in BST-325 composite films. When grains (initially separated by an insulating binder, pores, and voids) are merged and come in electrical contact on applying pressure, grain-boundary interfaces increase. The contacted grains increased mean free paths for charge carriers and facilitated hole transport. While increased interfaces helped scatter phonons and reduce thermal conductivity, which is discussed in detail in the thermal conductivity section.

The average density for the BST-100 composite films was 5.97 g/cm^3 , which is 88% of the bulk BST density [15,51]. These measurements confirm that the combination of fine and coarse particles in BST-100 packed very well and resulted in dense packing (closer to BST bulk density), thus improving the electrical conductivity [15,51]. By contrast, the average density of BST-325 composite films was 4.64 g/cm^3 and about 68% of the bulk BST density [15,51]. Therefore, the lower density of BST-325 composite films confirms the presence of pores (white arrows), which resulted in lower electrical conductivity [15,51,52].

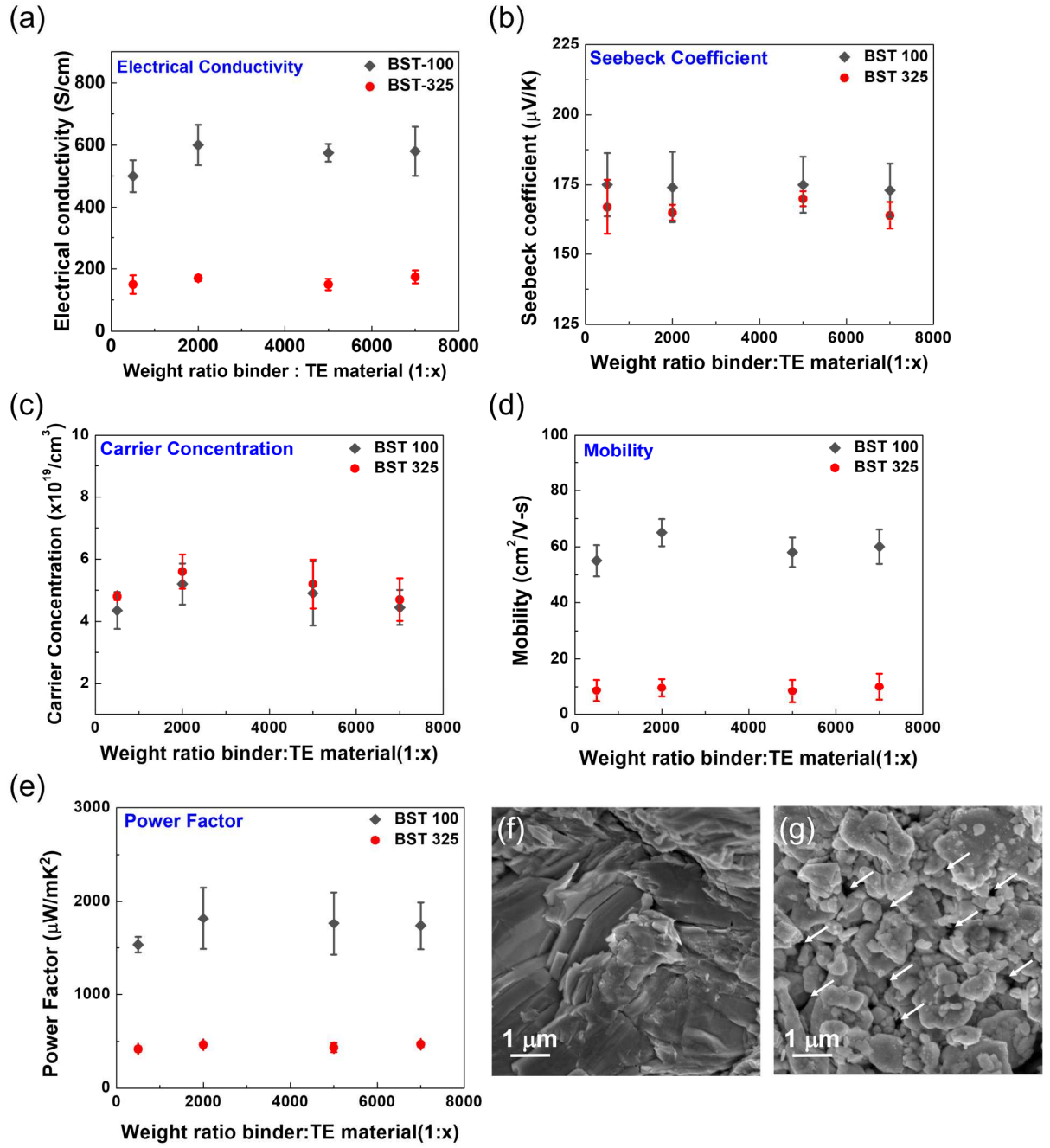


Fig. 3. (a) Electrical conductivity, (b) Seebeck coefficient, (c) charge carrier concentration, (d) mobility, and (e) power factor of chitosan-BST 100 and chitosan-BST 325 TE composite films with respect to the weight ratio of chitosan binder to TE particles (1:500, 1:2000, 1:5000, 1:7000), SEM images of (f) BST-100 TE composite film (1:2000 wt ratio), and (g) BST-325 TE composite film (1:2000 wt ratio).

2.4 Seebeck Coefficient and Power Factor

Fig. 3b shows the Seebeck coefficient of BST-100 and BST-325 TE composite films with respect to various binder-to-particle weight ratios. The positive Seebeck coefficient (160 -190 $\mu\text{V/K}$) confirms that the BST composite films are p-type TE. The Seebeck coefficient values of BST TE composite films did not show much variation when the binder-to-particle weight ratio or the particle size was changed. The average Seebeck coefficient of chitosan-BST TE composite films (174 $\mu\text{V/K}$) is comparable to bulk BST and printed BST films [15,20,36,38]. **Fig. 3c** shows the carrier concentration of chitosan-BST (100 and 325) TE composite films with respect to various binder-to-particle weight ratios. No significant change was observed in the carrier concentration of the chitosan-BST TE composite films on varying the particle size or the binder-to-particle weight ratio. The electrical conductivity σ is given by $\sigma = n e \mu$, where n is charge carrier concentration, μ is carrier mobility, and e is the elementary charge. The carrier concentration was similar for both BST-100 and BST-325 composite films. To understand the factors affecting the electrical conductivity, we performed carrier mobility measurements and found that the mobility of the BST-325 films (8-10 $\text{cm}^2/\text{V-s}$) was lower by orders of magnitude than the mobility of the BST-100 films (55-65 $\text{cm}^2/\text{V-s}$), as shown in **Fig. 3d**. The higher mobility of lower-mesh composites is due to the presence of big grains that result in a larger mean free path, as discussed above. The power factor of chitosan-BST (100 and 325) TE composite films with respect to various weight ratios of the binder were calculated as shown in **Fig. 3e**. The BST-100 composite films have a higher power factor (1550-2100 $\mu\text{W/mK}^2$) than BST-325 composite films (500-650 $\mu\text{W/mK}^2$) mainly because BST-100 composite films have higher electrical conductivity, as discussed above. Note that the average power factor (1810 $\mu\text{W/mK}^2$) of chitosan-BST-100 (1:2000) composite films is comparable to the printed BST TE

films reported in the literature, but without using high-temperature and long-duration sintering or a large amount of synthetic binder [14–20]. The comparison of power factor and ZT between naturally occurring chitosan binder (this study) vs. existing alternative binders (in previous literature) is presented in **Table S2 and S3**.

2.5 High-Temperature Thermoelectric Properties

The electrical conductivity and Seebeck coefficient of the chitosan-BST-100 (1:2000 wt. ratio) composite films at higher temperatures (25 °C, 50 °C, 75 °C, and 100 °C) are illustrated in **Fig. 4**. We chose these temperatures based on previous printable TEG studies targeting low waste-heat applications and reporting measurements of up to 100-125 °C [10,37,53]. Our printable and flexible TEG devices are also targeted for low waste-heat applications, which are globally in high demand. The average electrical conductivity of BST-100 composite films decreased from 600 S/cm to 500 S/cm with an increase in the temperature (25 °C to 100 °C), which shows the semi-metallic behavior of BST composite films (consistent with previous literature) [20,53]. The Seebeck coefficient did not change significantly on increasing the temperature. While the power factor of composite films decreased on increasing the temperature due to the decrease in electrical conductivity.

The application of pressure on the BST composite film may induce lattice strain (e.g., dislocations and interfaces), which may result in a change in density of states (DOS) effective mass, weighted mobility, and phonon vibrations [54,55]. Changes in the full width at half maximum (FWHM) and Raman shift of phonon modes (phonon softening) are informative of changes in DOS effective mass, weighted mobility, and phonon vibrations [54,55]. Therefore, we performed Raman analysis to examine pressure-induced defects. In BST powder and BST films, all Raman active BST

vibration (phonon) modes A_{1g}^1 , E_g , and A_{1g}^2 (66, 108, 168 cm^{-1}) are observed (**Fig. 2c**) [42, 54,55]. However, the E_g peak shifted from 108 cm^{-1} for the BST powder sample to 118 cm^{-1} for the BST film sample (**Fig. 2c**). In addition, FWHM comparison of the E_g peak of BST powder and chitosan-BST-100 composite films (at 200 MPa applied pressure) (**Fig. 2d**) shows the FWHM increased on the application of pressure. The peak shift and increased FWHM suggest defects were introduced in the composite film on applying pressure. The Raman peak shift and increase in FWHM indicate a change in DOS effective mass and weighted mobility and increased phonon vibrations [54–56].

In addition, we substituted measured electrical conductivity and Seebeck coefficient (for BST-100 composite films prepared using different applied pressure) in the Snyder equation to calculate the weighted mobility [56]. The calculated weighted mobility of BST-100 composite films was 192 $\text{cm}^2/\text{V-s}$ (at 200 MPa) and 50 $\text{cm}^2/\text{V-s}$ (at 100 MPa). The higher weighted mobility of BST-100 composite films at 200 MPa compared to 100 MPa applied pressure suggests that DOS effective mass is higher for BST-100 composite films at higher applied pressure [56,57]. We also calculated the DOS effective mass using the calculated weighted mobility and measured Hall mobility [56]. It is observed that DOS effective mass for 200 MPa film ($2.3m_e$) is slightly higher than 100 MPa film ($2.24m_e$), confirming a higher density of electron states for the 200 MPa film. Furthermore, the deformation potential phonon scattering theory suggests the decrease in weighted mobility occurs with temperature as $T^{-3/2}$ [56]. Therefore, the weighted mobility of BST-100 composite films (at 200 MPa) was calculated using measured high temperature (25-100 $^{\circ}\text{C}$) electrical conductivity and Seebeck coefficient. As shown in **Fig. 4d**, the weighted mobility decreased with increased temperature [56,57]. This trend is consistent with the prediction of deformation potential phonon scattering theory and existing literature [57].

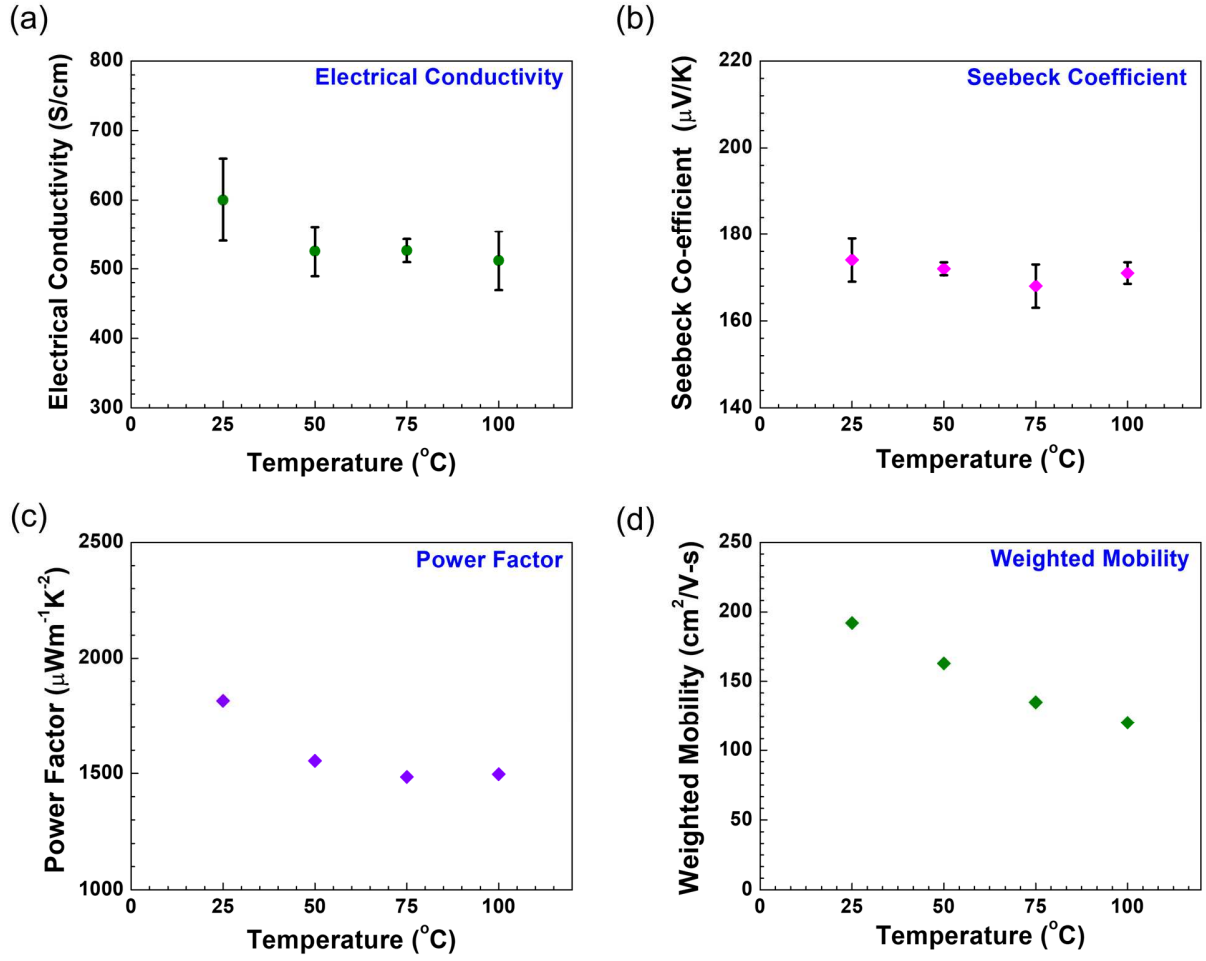


Fig. 4. (a) Electrical conductivity, (b) Seebeck coefficient, (c) power factor, and (d) weighted mobility of chitosan- BST-100 films (1:2000 wt. ratio) at 200 MPa at different temperatures

2.6 Thermal Conductivity

The measured in-plane and out-of-plane thermal conductivity of BST-100 films were 0.78 W/m-K and 0.74 W/m-K, respectively. The in-plane and out-of-plane thermal conductivity are almost the same (i.e., thermal conductivity is isotropic) because BST grains are randomly oriented (polycrystalline nature) in chitosan-BST composite films [14,18,19,36,58–60]. Therefore, to confirm the random orientation of BST grains in the chitosan-BST composite

films, HRTEM and SAED analyses were performed on BST composite films (**Fig. S6a-g**) and detailed explanation is in supplementary file [58-62].

The measured thermal conductivity of the BST-100 composite films is almost half of the bulk BST value. It is similar to previous reports on binder-based printed TE composite films [14,23,24,38,53,63]. It is also less than the thermal conductivity of removable binder-based printed BST composite films (0.9-1.5 W/m-K) [15–20,36]. The calculated lattice thermal conductivity of BST-100 composite film was 0.31 W/m-k, approximately 30% of the BST bulk lattice conductivity (1.04 W/m-K) [18,36,64]. The low lattice thermal conductivity (which contributes to low thermal conductivity) of BST-100 composite films can be attributed to the presence of (1) size and density of nano-sized defects (TE particles and pores) (2), insulating chitosan binder, (3) grain-grain and grain-polymer interfaces, and (4) weak bonds. Below, we examine the effect of each of these four factors on phonon scattering and low lattice thermal conductivity.

Dresselhaus et al. (1993) suggested that nano-structuring can help reduce thermal conductivity and enhance electrical conductivity and ZT [65,66]. BST-100 composite films have a combination of micron-sized and nano-sized TE particles. The size distribution of nanoparticles and pores was estimated using FESEM of BST-100 films (inset in **Fig. 5a**) as shown in **Fig. 5a-b**. The average TE particle size was estimated to be ~7 nm (for ~14000 particles in a 1.91 μ m \times 1.25 μ m area) in the BST-100 film (**Fig. 5a**). Using the same FESEM scan, the average pore size was estimated to be 5 nm (for ~15000 pores) (**Fig. 5b**). The BET analysis also confirmed the pore diameter of about 4 nm for BST-100 composite films, as shown in **Fig. 5c-d**. In addition, the BET analysis indicates that the volume% of nanopores is about 1%. The N₂ adsorption-desorption isotherm curve (**Fig. 5c**) shows typical type IV isotherm corresponding to

a mesoporous material (pore diameter between 2 nm and 50 nm), confirming the presence of nanoscale pores [49,63,65,66]. The presence of nanoscale TE particles and pores in BST composite film can effectively scatter phonons, resulting in lower thermal conductivity [53]. Hellman et al. (2014) also show that the lattice thermal conductivity of Bi_2Te_3 decreases to less than $0.3\text{W/m}\cdot\text{K}$ when the phonon mean free path is about 1.5nm [67]. The nano-sized TE particles and pores are smaller than the phonon mean free path, which causes phonon scattering [36,53,63,65-68]. However, the size of big grains is larger than the electron mean free path, which reduces charge-carrier scattering and contributes to high mobility and electrical conductivity, as discussed above.

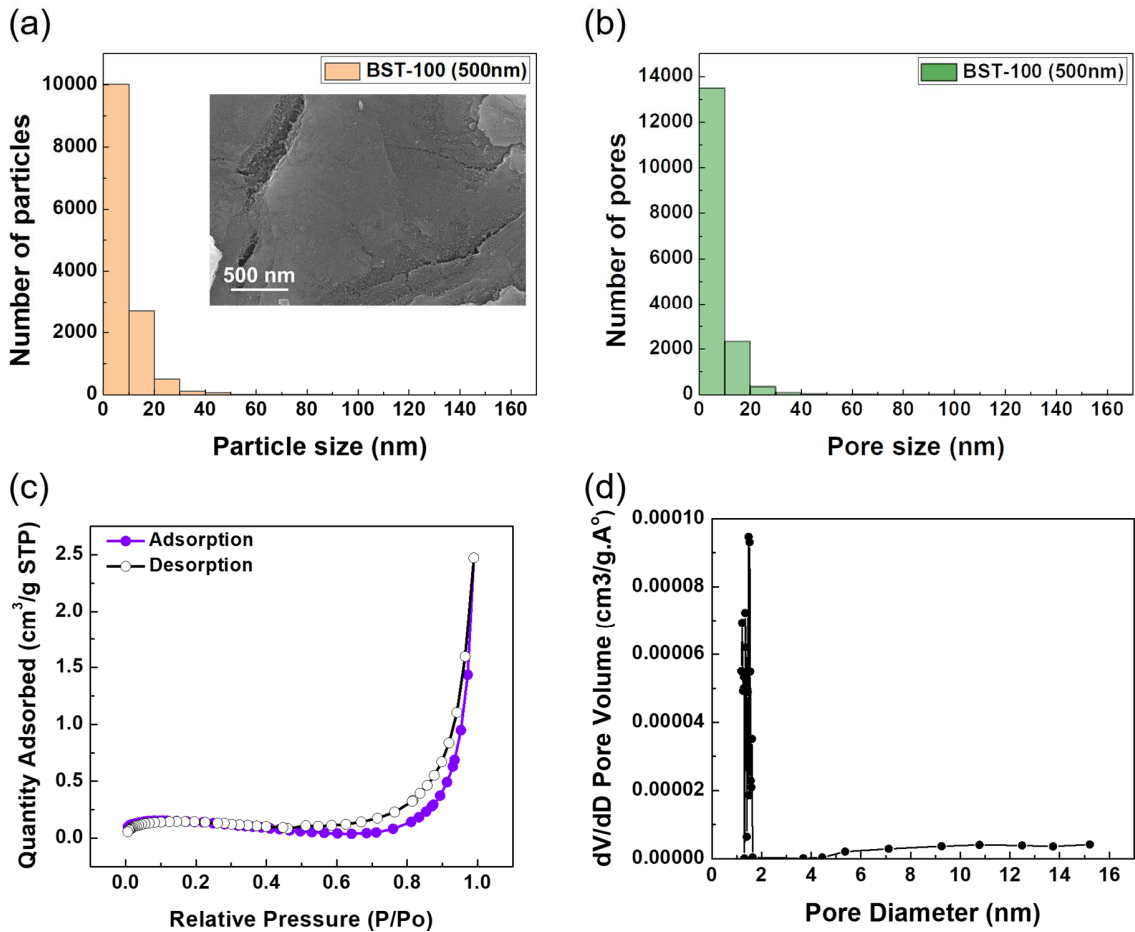


Fig. 5. (a) Nano-sized TE particle count vs. particle size using FESEM image of Chitosan-BST-100 composite films (shown in inset), (b) nanoscale void size vs. particle size, using ImageJ software for counting the particles and pores, (c) Nitrogen adsorption-desorption isotherms of BST-100 composite films, (d) void size distribution of BST-100 composite films obtained from BET analysis.

Nan et al. (2004) theoretically showed that a large interfacial thermal resistance exists across micro/nano features in composite films [68]. Moreover, many researchers have experimentally shown that in polymer-particle composite films, particle-particle and particle-polymer interfaces increase the interfacial thermal resistance and help lower the thermal conductivity of the composite film [69–74]. In this work, a small amount (0.05 wt.%) of chitosan binder appears in inter-grain nano-range spacing, facilitating interfacial resistance around the TE particles as shown in HRTEM images (**Fig. 6a-c**). The dense packing of heterogenous TE particles in BST-100 composite films helps in spreading the polymer binder (white interfaces) uniformly around the TE particles (black particles) and creates polymer-particle interfaces (**Fig. 6a-c**). The presence of polymer-particle interfaces and particle-particle interfaces in BST composite films resulted in increased interfacial thermal resistance and reduced lattice thermal conductivity due to phonon scattering [53,63,68–74]. The HRTEM image of BST-100 powder did not show the presence of chitosan interfaces (**Fig. 6d-f**). The EDAX elemental mapping, spot EDAX, and corresponding elemental line profile of BST-chitosan composite film confirm the homogenous distribution of Bi, Sb, Te, C, O, and N, respectively (**Fig. S8-10**). Therefore, the detailed EDAX analysis manifested the presence of polymer-particle interfaces and particle-particle interfaces in BST composite films, as shown in the HRTEM image (**Fig. 6**).

Lee et al. (2021) predict the interactive role of nanodefekt types in reducing lattice thermal conductivity and show that lattice thermal conductivity can be reduced to 0.35W/m-K if

there is the combination of an average grain size of 10nm and a small wt% of nanoparticles (about 0.2 wt%) [75]. As shown in the HRTEM (**Fig. 6**), EDAX (**Fig. S8-S10**), FESEM, and BET (**Fig. 5**) images, 2D (grain boundaries) and 3D (nanoparticles and pores) nanodefects are present in chitosan-BST100 composite films. The average TE particle size was estimated to be ~7 nm (for ~14000 particles in a $1.91\mu\text{m}\times 1.25\mu\text{m}$ area) in the BST-100 film (**Fig. 5a**). Using the same FESEM scan, the average pore size was estimated to be 5 nm (for ~15000 pores) (**Fig. 5b**). The BET analysis indicates that the volume% of nanopores is about 1% (**Fig 5 c-d**). The grain boundaries and nanodefects present in the chitosan-BST composite contribute to the low lattice thermal conductivity [75].

The weak bonds formed at particle-particle interfaces (due to uniaxial applied pressure and plastic deformation of particles) will scatter phonons but not electrons, reducing lattice thermal conductivity [76]. These results demonstrate that our energy-efficient process successfully enhanced electrical conductivity and reduced thermal conductivity. The ZT of the best performing chitosan-BST-100 composite films (1:2000 wt ratio) was about 0.7 at room temperature and is comparable to the best reported ZT of printed BST TE films [12–15,20,53].

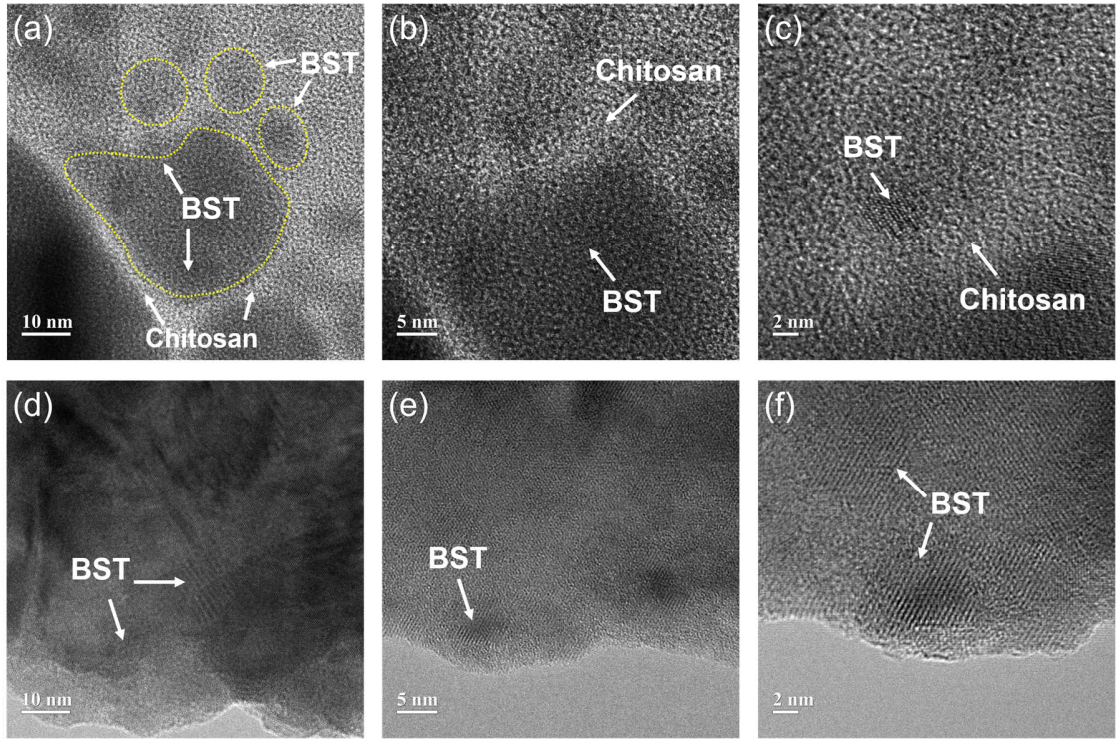


Fig. 6. (a-c) HRTEM images of chitosan-BST-100 composite films at various magnifications showing the presence of chitosan binder interfaces, (d-f) BST powder (no chitosan interfaces).

A 3-leg BST TEG device was stencil-printed using BST-100 (1:2000 wt ratio) as shown in **Fig. 7** with thermoelement dimensions of $5\text{mm} \times 7\text{mm} \times 70\mu\text{m}$ (*length* \times *width* \times *thickness*) [10,13,64]. The voltage and power output characterizations were performed at room temperature, as shown in **Fig. 7**. The measured TEG open-circuit voltage increased linearly with ΔT and is comparable to the ideal open-circuit voltage calculated using a Seebeck coefficient of BST-100 films (**Fig. 7a**). The maximum power output of $58\text{ }\mu\text{W}$ was achieved at ΔT of 38 K with a closed-circuit voltage of 10 mV and a current of 6 mA (**Fig. 7b**). The maximum device power density of 3.5 mW/cm^2 was obtained at ΔT of 38 K (**Fig. 7c**) [38,39]. The corresponding power density was 5.72 mW/cm^2 when the area between thermoelements was not included [20]. The increase in the gap between the ideal and measured power density curves with ΔT can be

attributed to increased device electrical resistance with temperature. The TEG device fabricated using an energy-efficient method achieved an ultra-high-power density which is among the best reported for single-leg TEG devices (**Table S4**). The flexibility of this device was performed (**Fig. 7d**) and details in supplementary file. These devices can potentially be used as self-sufficient and long-lasting power supplies for powering sensors and charging batteries in individual and miniature next-generation wearable device applications.

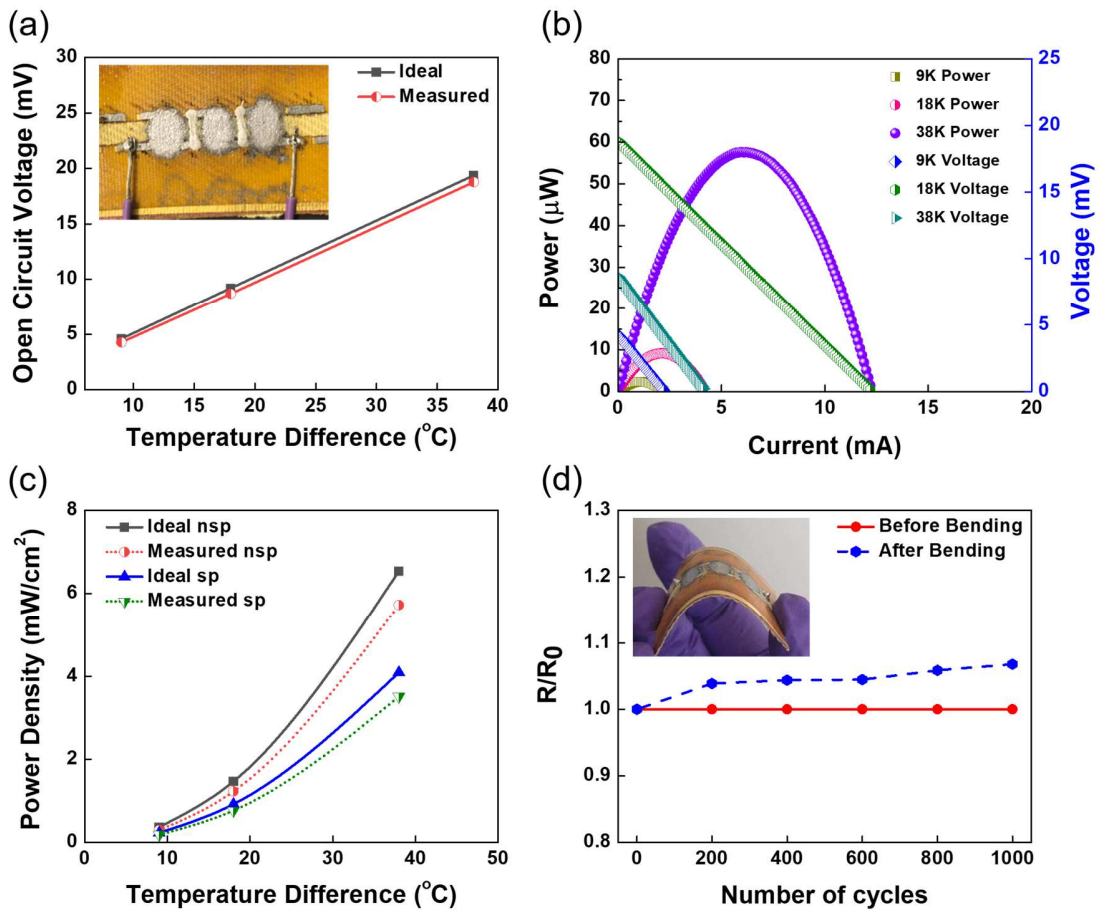


Fig. 7: Characterization results of a three-element TEG prototype: (a) ideal and measured open-circuit voltage vs. temperature difference (ΔT), (b) TEG voltage and power curve at ΔT of 9 K, 18 K, and 38 K, (c) ideal and measured power density at various ΔT , with (sp) and without (nsp) including the spacing area, (d) normalized resistance of TEG vs. bending cycles. Here, R_0 and R are resistance before and after bending.

Conclusions

In summary, this work demonstrates the feasibility of using an inexpensive and energy-efficient method of fabricating flexible, printable TEGs, eliminating the need for an energy-intensive (long-duration and high-temperature) curing process to increase the mean free path for charge carriers. An energy-efficient approach combines (1) a small amount of naturally occurring binder (0.05 wt%) sufficient to hold the TE particles together in the film without significantly decreasing the electrical conductivity. (2) The heterogeneous distribution of particle sizes (a unique combination of micro and nanoparticles) packed very well (3) on the application of uniaxial pressure (4) at low curing temperature (150 °C) and short duration (30 minutes) yields big grains larger than the mean free path for charge carriers (high electrical conductivity), and nano features smaller than the mean free path for phonons (low thermal conductivity). Using this approach, the chitosan-BST-100 TE composite films achieved a power factor of 1810 $\mu\text{W}/\text{mK}^2$, thermal conductivity of 0.78 W/m-K, and ultrahigh ZT of 0.7 at room temperature. The ZT achieved is among the best reported ZT for printed composite films without using high-temperature and long-duration curing. The power density of 3-leg-BST TEG is 5.7 mW/cm² at a temperature difference of 38 K, which is significantly higher than the best-reported power density values for single-leg TEG devices at the same temperature difference. The bending test at a 3-cm radius for 1000 cycles demonstrated the excellent flexibility of this prototype device. We envisage that the energy-efficient process, flexible, and cost-effective printable strategy presented in this work pave the way for manufacturing large-scale and high-performance energy harvesting thermoelectric devices.

Notes

The authors declare no competing interest

Acknowledgment

The authors would like to thank Aakash Sathish from Reservoir High School and Preetham Gowni from Mount Hebron High School for their contributions. Thank you to Prof. Erin Lavik for letting us use their Keyence microscope. This work was supported by Dr. D. Madan's startup fund from the University of Maryland Baltimore County, Baltimore. M. S. and Y. Z. would like to acknowledge funding support from the National Science Foundation under award CMMI-1747685.

References

- [1] A.F. Ioffe, L.S. Stil'bans, E.K. Iordanishvili, T.S. Stavitskaya, A. Gelbtuch, G. Vineyard, Semiconductor Thermoelements and thermoelectric cooling, *Phys. Today* 12 (5) (1959) 42.
- [2] G.J. Snyder, E.S. Toberer, Complex thermoelectric materials, *Mater. Sustain. Energy* 7 (2010) 101–110.
- [3] A. Majumdar, Thermoelectricity in semiconductor nanostructures, *Science* 303 (5659) (2004) 777–778.
- [4] T.M. Tritt, M.A. Subramanian, Thermoelectric materials, phenomena, and applications: A bird's eye view, *MRS Bulletin* 31 (2006) 188–198.
- [5] S. Leblanc, S.K. Yee, M.L. Scullin, C. Dames, K.E. Goodson, Material and manufacturing cost considerations for thermoelectrics, *Renew Sustain. Energy Rev.* 32 (2014) 313–327.
- [6] R. Venkatasubramanian, E. Siivola, T. Colpitts, B. O'Quinn, Thin-film thermoelectric devices with high room-temperature figures of merit, *Nature* 413 (2011) 597–602.
- [7] D. Madan, X. Zhao, R.M. Ireland, D. Xiao, H.E. Katz, Conductivity and power factor enhancement of n-type semiconducting polymers using sodium silica gel dopant, *APL Materials* 5 (2017), 086106.
- [8] X. Zhao, D. Madan, Y. Cheng, J. Zhou, H. Li, S.M. Thon, A.E. Bragg, M.E. DeCoster, P.E. Hopkins, H.E. Katz, High conductivity and electron-transfer validation in an n-type fluoride-anion-doped polymer for thermoelectrics in air, *Adv. Mater.* 29 (34) (2017), 1606928.
- [9] A. Chen, D. Madan, M. Koplow, P.K. Wright, J.W. Evans, Dispenser printed thermoelectric energy generators, *Proc PowerMEMS* (2009) 277–280.
- [10] D. Madan, Z. Wang, P.K. Wright, J.W. Evans, Printed flexible thermoelectric generators for use on low levels of waste heat, *Appl. Energy* (156) 2015 587–92.
- [11] E. Jang, A. Poosapati, N. Jang, L. Hu, M. Duffy, M. Zupan, D. Madan, Thermoelectric properties enhancement of p-type composite films using wood-based binder and mechanical pressing, *Sci Rep.* 9 (2019), 7869.
- [12] D. Madan, Z. Wang, A. Chen, R. Winslow, P.K. Wright, J.W. Evans, Dispenser printed

- circular thermoelectric devices using Bi and Bi_{0.5}Sb_{1.5}Te₃, *Appl. Phys. Lett.* 104 (2014), 013902.
- [13] A. Chen, D. Madan, P.K. Wright, J.W. Evans, Dispenser-printed planar thick-film thermoelectric energy generators, *J. Micromechanics Microengineering* 21 (10) (2011), 104006.
 - [14] D. Madan, A. Chen, P.K. Wright, J.W. Evans, Dispenser printed composite thermoelectric thick films for thermoelectric generator applications, *J. Appl. Phys.* 109 (2011), 034904.
 - [15] H. Choi, Y.J. Kim, C.S. Kim, H.M. Yang, M.W. Oh, B.J. Cho, Enhancement of reproducibility and reliability in a high-performance flexible thermoelectric generator using screen-printed materials, *Nano Energy* 46 (2018) 39–44.
 - [16] S.J. Kim, H. Choi, Y. Kim, J.H. We, J.S. Shin, H.E. Lee, M.W. Oh, K.J. Lee, B.J. Cho, Post ionized defect engineering of the screen-printed Bi₂Te_{2.7}Se_{0.3} thick film for high performance flexible thermoelectric generator, *Nano Energy* 31 (2017) 258–263.
 - [17] T. Varghese, C. Hollar, J. Richardson, N. Kempf, C. Han, P. Gamarrachchi, D. Estrada, R.J. Mehta, Y. Zhang, High-performance and flexible thermoelectric films by screen printing solution-processed nanoplate crystals, *Sci Rep* 6 (2016), 33135.
 - [18] S. Shin, R. Kumar, J.W. Roh, D.S. Ko, H.S. Kim, S.I. Kim, L. Yin, S.M. Schlossberg, S. Cui, J.M. You, S. Kwon, J. Zheng, J. Wang, R. Chen, High-performance screen-printed thermoelectric films on fabrics, *Sci Rep* 7 (2017), 7317.
 - [19] S.J. Kim, J.H. We, B.J. Cho, A wearable thermoelectric generator fabricated on a glass fabric, *Energy Environ. Sci.* 7 (2014) 1959–1965.
 - [20] T. Varghese, C. Dun, N. Kempf, M. Saeidi-Javash, C. Karthik, J. Richardson, C. Hollar, D. Estrada, Y. Zhang, Flexible thermoelectric devices of ultrahigh power factor by scalable printing and interface engineering, *Adv. Funct. Mater.* 30 (5) (2019), 1905796.
 - [21] J. Huang, H. Li, E. Kirksey, C. Hoffman, H. Jang, J. Wagner, D. Madan, H.E. Katz, Contributions to composite conductivity and Seebeck coefficient in commercial Bi₂Te₃ — Conjugated polymer composites, *J. Appl. Phys* 125 (2019), 125502.
 - [22] E. Jang, A. Poosapati, D. Madan, Enhanced thermoelectric properties of F4TCNQ doped P3HT and its use as a binder for Sb₂Te₃ based printed thermoelectric films, *ACS Appl. Energy Mater* 1 (4) (2018), 1455–1462.
 - [23] E. Jang, P. Banerjee, J. Huang, R. Holley, J.T. Gaskins, M.S. Bin Hoque, P.E. Hopkins, D. Madan, Thermoelectric performance enhancement of naturally occurring bi and chitosan composite films using energy efficient method. *Electron* 9 (2020) 1–12.
 - [24] P. Banerjee, E. Jang, J. Huang, R. Holley, S. Vadnala, A. Sheikh, A. Trivedi, K. Jackson, V.K. Homman, D. Madan, Thermoelectric performance enhancement of n-type chitosan-Bi₂Te_{2.7}Se_{0.3} composite films using heterogeneous grains and mechanical pressure, *J. Electron. Mater.* 50 (2021) 2840–2851.
 - [25] B. Du, S. Hu, R. Singh, T. Tsai, C. Lin, F. Ko, Eco-friendly and biodegradable biopolymer Chitosan/Y₂O₃ composite materials in flexible organic thin-film transistors, *Materials* 10 (9) (2017), 1026.

- [26] N.R. Hosseini, J. Lee, Biocompatible and flexible chitosan-based resistive switching memory with magnesium electrodes, *Adv. Funct. Mater.* 25 (35) (2015) 5586–5592.
- [27] D. Yang, Y. Wang, L. He, H. Li, Carboxyl-functionalized ionic liquid assisted preparation of flexible, transparent, and luminescent chitosan films as vapor luminescent sensor, *ACS Appl. Mater. Interfaces* 8 (30) (2016) 19709–19715.
- [28] C.G.T. Neto, J.A. Giacometti, A.E. Job, F.C. Ferreira, J.L.C. Fonseca, M.R. Pereira, Thermal analysis of chitosan based networks, *Carbohydr. Polym.* 62 (2) (2005) 97–103.
- [29] R. Clark, B. Averbach, The mechanical properties of chitosan membranes, *Proc. Oceans* (1978) 82–86.
- [30] A. Poosapati, S. Vadnala, K. Negrete, Y. Lan, J. Hutchison, M. Zupan, D. Madan, Rechargeable zinc-electrolytic manganese dioxide (EMD) battery with a flexible chitosan-alkaline electrolyte, *ACS Appl. Energy Mater.* 4 (4) (2021) 4248–4258.
- [31] A. Poosapati, K. Negrete, M. Thorpe, J. Hutchison, M. Zupan, Y. Lan, D. Madan, Safe and flexible chitosan-based polymer gel as an electrolyte for use in zinc-alkaline based chemistries, *J. Appl. Polym. Sci.* (2021), 50813.
- [32] T. Fukui, M. Matsuzawa, R. Funahashi, A. Kosuga, Effect of mixed grain sizes on the thermoelectric properties of $\text{Ca}_{0.9}\text{Yb}_{0.1}\text{MnO}_3$, *J. Electron Mater.* 43 (2014) 1548–1553.
- [33] L.D. Zhao, B.P. Zhang, W.S. Liu, J.F. Li, Effect of mixed grain sizes on thermoelectric performance of Bi_2Te_3 compound, *J. Appl. Phys.* 105 (2009), 023704.
- [34] K. Kishimoto, T. Koyanagi, Preparation of sintered degenerate n-type PbTe with a small grain size and its thermoelectric properties, *J. Appl. Phys.* 92 (2002) 2544–2549.
- [35] S. Fan, J. Zhao, J. Guo, Q. Yan, J. Ma, H.H. Hng, P-type $\text{Bi}_{0.4}\text{Sb}_{1.6}\text{Te}_3$ nanocomposites with enhanced figure of merit, *Appl. Phys. Lett.* 96 (2010), 182104.
- [36] B. Poudel, Q. Hao, Y. Ma, Y. Lan, A. Minnich, B. Yu, X. Yan, D. Wang, A. Muto, D. Vashaee, X. Chen, J. Liu, M.S. Dresselhaus, G. Chen, Z. Ren, High-thermoelectric performance of nanostructured bismuth antimony telluride bulk alloys. *Science* 320 (2008) 634–638.
- [37] D. Madan, A. Chen, P.K. Wright, J.W. Evans, Printed Se-doped MA n-Type Bi_2Te_3 thick-film thermoelectric generators, *J. Electron. Mater.* 41 (2012) 1481–1486.
- [38] D. Madan, Z. Wang, A. Chen, P.K. Wright, J.W. Evans, High-performance dispenser printed MA p-type $\text{Bi}_{0.5}\text{Sb}_{1.5}\text{Te}_3$ flexible thermoelectric generators for powering wireless sensor networks, *ACS Appl. Mater. Interfaces* 5 (22) (2013) 11872–11876.
- [39] D. Madan, Z. Wang, A. Chen, R.C. Juang, J. Keist, P.K. Wright, J.W. Evans, Enhanced performance of dispenser printed MA n-type Bi_2Te_3 composite thermoelectric generators, *ACS Appl. Mater. Interfaces* 4 (11) (2012) 6117–6124.
- [40] D. Suh, S. Lee, H. Mun, S. Park, K.H. Lee, S.W. Kim, J. Choi, S. Baik, Enhanced thermoelectric performance of $\text{Bi}_{0.5}\text{Sb}_{1.5}\text{Te}_3$ -expanded graphene composites by simultaneous modulation of electronic and thermal carrier transport, *Nano Energy* 13 (2015) 67–76.
- [41] S.W. Ali, S. Rajendran, M. Joshi, Synthesis and characterization of chitosan and silver loaded chitosan nanoparticles for bioactive polyester, *Carbohydr. Polym.* 83 (2) (2011) 438–446.

- [42] G. Zheng, X. Su, H. Xie, Y. Shu, T. Liang, X. She, W. Liu, Y. Yan, Q. Zhang, C. Uher, M. G. Kanatzidis, X. Tang, High thermoelectric performance of p-BiSbTe compounds prepared by ultra-fast thermally induced reaction, *Energy Environ. Sci.* 10 (2017) 2638-2652.
- [43] D. Han, T. Han, C. Shan, A. Ivaska, L. Niu, Simultaneous determination of ascorbic acid, dopamine and uric acid with chitosan-graphene modified electrode, *Electroanalysis* 22 (2010) 2001–2008.
- [44] E. Szymańska, K. Winnicka, Stability of chitosan - A challenge for pharmaceutical and biomedical applications, *Mar. Drugs* 13 (4) (2015) 1819–1846.
- [45] I. Corazzari, R. Nisticò, F. Turci, M.G. Faga, F. Franzoso, S. Tabasso, G. Magnacca, Advanced physico-chemical characterization of chitosan by means of TGA coupled on-line with FTIR and GCMS: Thermal degradation and water adsorption capacity, *Polym. Degrad. Stab.* 112 (2015) 1–9.
- [46] D.S. McLachlan, M. Blaszkiewicz, R.E. Newnham, Electrical resistivity of composites, *J. Am. Ceram. Soc.* 73 (8) (1990) 2187–2203.
- [47] M. Hussain, Y.H. Choa, K. Niihara, Fabrication process and electrical behavior of novel pressure-sensitive composites, *Compos. - Part A Appl. Sci. Manuf.* 32 (12) (2001) 1689–1696.
- [48] C. Nan, Physics of inhomogeneous inorganic materials, *Prog. Mater. Sci.* 37 (1) (1993) 1–116.
- [49] Y.P. Mamunya, V.V. Davydenko, P. Pissis, E.V. Lebedev, Electrical and thermal conductivity of polymers filled with metal powders, *Eur. Polym. J.* 38 (9) (2002) 1887–1897.
- [50] A. Gharleghi, Y. Liu, M. Zhou, J. He, T.M. Tritt, C. Liu, Enhancing the thermoelectric performance of nano-sized CoSb₃: Via short-range percolation of electrically conductive WTe₂ inclusions, *J. Mater. Chem. A* 4 (2016) 13874–13880.
- [51] Y.Y. Li, X.Y. Qin, D. Li, J. Zhang, C. Li, Y.F. Liu, et al. Enhanced thermoelectric performance of Cu₂Se/Bi_{0.4}Sb_{1.6}Te₃ nanocomposites at elevated temperatures, *Appl. Phys. Lett.* 108 (2016), 062104.
- [52] M. Kashiwagi, S. Hirata, K. Harada, Y. Zheng, K. Miyazaki, M. Yahiro, C. Adachi, Enhanced figure of merit of a porous thin film of bismuth antimony telluride. *Appl. Phys. Lett.* 98 (2011), 023114.
- [53] S.H. Park, S. Jo, B. Kwon, F. Kim, H.W. Ban, J.E. Lee, D.H. Gu, S.H. Lee, Y. Hwang, J. Kim, D. Hyun, S. Lee, K.J. Choi, W. Jo, J.S. Son, High-performance shape-engineerable thermoelectric painting, *Nat. Commun.* 7 (2016), 13403.
- [54] D.A. Polvani, J.F. Meng, N.V. Chandra Sekhar, J. Sharp, J.V. Badding, Large improvement in thermoelectric properties in pressure-tuned p-type Sb_{1.5}Bi_{0.5}Te₃, *Chem. Mater.* 13 (2001) 2068-2071
- [55] Z. Wu, X. Chen, E. Mu, Y. Liu, Z. Che, C. Dun, F. Sun, X. Wang, Y. Zhang, Z. Hu, Lattice strain enhances thermoelectric properties in Sb₂Te₃/Te heterostructure, *Adv. Electron. Mater.* (2019), 1900735.
- [56] G.J. Snyder, A.H. Snyder, M. Wood, R. Gurunathan, B.H. Snyder, C. Niu, Weighted mobility, *Adv. Mater.* 32 (2020), 2001537.
- [57] I.T. Witting, F. Ricci, T.C. Chasapis, G. Hautier, G.J. Snyder, The thermoelectric properties of N-type bismuth telluride: bismuth selenide alloys Bi₂Te_{3-x} Sex, *Research* 2020 (2020), 4361703.

- [58] C.-H. Chien, P.-C. Lee, W.-H. Tsai, C.-H. Lin, C.-H. Lee, Y.-Y. Chen, In-situ observation of size and irradiation effects on thermoelectric properties of Bi-Sb-Te nanowire in FIB trimming, *Sci. Rep.* 6 (2016), 23672.
- [59] M. Scheele, N. Oeschler, K. Meier, A. Kornowski, C. Klinke, H. Weller, Synthesis and thermoelectric characterization of Bi₂Te₃ nanoparticles, *Adv. Funct. Mater.* 19 (2009) 3476–3483.
- [60] H. Ju, J. Kim, Preparation and structure dependent thermoelectric properties of nanostructured bulk bismuth telluride with graphene, *J. Alloys Compd.* 664 (2016) 639–647.
- [61] D. R. Askeland, Atomic and Ionic Arrangements, in: D.R. Askeland, *The Science and Engineering of Materials*, third ed.; PWS Publishing Company, Boston, 1994, pp. 75–76.
- [62] K. Shen, Z.-H. Huang, K. Hu, W. Shen, S. Yu, J. Yang, G. Yang, F. Kang, Advantages of natural microcrystalline graphite filler over petroleum coke in isotropic graphite preparation. *Carbon* 90 (2015) 197.
- [63] E. Jang, P. Banerjee, J. Huang, D. Madan, High performance scalable and cost-effective thermoelectric devices fabricated using energy efficient methods and naturally occurring materials, *Appl. Energy* 294 (2021), 117006.
- [64] H. Kim, Z.M. Gibbs, Y. Tang, H. Wang, G.J. Snyder, Characterization of Lorenz number with Seebeck coefficient measurement measurement, *APL Mater.* 3 (2015), 041506.
- [65] L. Hicks, M.S. Dresselhaus, Thermoelectric figure of merit of a one-dimensional conductor, *Phys. Rev. B Condens. Matter.* 47 (24) (1993) 16631–16634.
- [66] A.J. Minnich, M.S. Dresselhaus, Z.F. Ren, G. Chen, Bulk nanostructured thermoelectric materials: Current research and future prospects, *Energy Environ. Sci.* 2 (2009), 466–479.
- [67] O. Hellman, D.A. Broido, Phonon thermal transport in Bi₂Te₃ from first principles, *Phy. Rev. B* 90 (2014), 134309.
- [68] C.W. Nan, G. Liu, Y. Lin, M. Li, Interface effect on thermal conductivity of carbon nanotube composites, *Appl. Phys. Lett.* 85 (2004), 3549.
- [69] C. Meng, C. Liu, S. Fan, A promising approach to enhanced thermoelectric properties using carbon nanotube networks, *Adv. Mater.* 22 (4) (2010) 535–539.
- [70] D. Portehault, V. Maneeratana, C. Candolfi, N. Oeschler, I. Veremchuk, Y. Grin, C. Sanchez, M. Antonietti, Facile general route toward tunable magnéli nanostructures and their use as thermoelectric metal oxide/carbon nanocomposites, *ACS Nano* 5 (11) (2011) 9052–9061.
- [71] S. Ganguly, C. Zhou, D. Morelli, J. Sakamoto, S.L. Brock, Synthesis and characterization of telluride aerogels: Effect of gelation on thermoelectric performance of Bi₂Te₃ and Bi_{2-x}Sb_xTe₃ nanostructures, *J. Phys. Chem. C* 116 (33) (2012) 17431–17439.
- [72] C. Jiang, P. Wei, Y. Ding, K. Cai, L. Tong, Q. Gao, Y. Lu, W. Zhao, S. Chen, Ultrahigh performance polyvinylpyrrolidone/Ag₂Se composite thermoelectric film for flexible energy harvesting, *Nano Energy* 80 (2021), 105488.
- [73] S. Sahoo, V.R. Chitturi, R. Agarwal, J.W. Jiang, R.S. Katiyar, Thermal conductivity of freestanding single wall carbon nanotube sheet by Raman spectroscopy, *ACS Appl. Mater. Interfaces* 6 (22) (2014) 19958–19965.
- [74] S.I. Kim, H.A. Mun, H.S. Kim, S.W. Hwang, J.W. Roh, D.J. Yang, W.H. Shin, X.S. Li, Y.H. Lee, G.J. Snyder, S.W. Kim, Dense dislocation arrays embedded in grain boundaries for high-performance bulk thermoelectrics, *Science* 348 (2015) 109–114.
- [75] K. H. Lee, Y.-M. Kim, C. O. Park, W. H. Shin, S. W. Kim, H.-S. Kim, S. I. Kim, Cumulative defect structures for experimentally-attainable low thermal conductivity in thermoelectric (Bi,

Sb)₂Te₃ alloys, Mater. Today Energy 21 (2021), 100795.

- [76] C. Yu, Y.S. Kim, D. Kim, J.C. Grunlan, Thermoelectric behavior of segregated-network polymer nanocomposites, Nano Lett. 8 (12) (2008) 4428–4432.

High performing p-type Chitosan-BST composite films were synthesized using energy efficient methods (wide distribution of particle sizes, the weight ratio of polymer binder, and external uniaxial pressure). Using these composite inks highly scalable and flexible thermoelectric generator were fabricated and achieved ultra-high-power density of 5.72 mW/cm^2 .

